PAPER

Check for updates

PAR-intercalated Mg/Al layered double hydroxide for efficient adsorption of acid fuchsin: experimental study and molecular docking insights

Sara E. Abdel Hameed, Weam M. Abou El-Maaty, Esam A. Gomaa
and Fathi S. Awad [ID] *

This study systematically investigated the adsorptive removal of acid fuchsin (AF), an anionic dye, from aqueous solutions using a 4-(2-pyridylazo)resorcinol-intercalated magnesium/aluminum layered double hydroxide (PAR-Mg/Al LDH). The composite was successfully synthesized and characterized by FTIR, XRD, SEM, EDX, and XPS. Batch adsorption experiments demonstrated that PAR intercalation significantly enhanced the adsorption performance compared to pristine Mg/Al LDH. Key parameters influencing the adsorption process, including contact time, initial dye concentration, pH, and temperature, were systematically optimized. The adsorption isotherm data were best described by the Langmuir model, indicating monolayer adsorption with a high maximum capacity of 568.18 mg g^{-1}. Kinetic studies revealed that the adsorption process followed the pseudo-second-order model, with excellent agreement between experimental and calculated adsorption capacities. Further kinetic analysis using intraparticle diffusion and Boyd models demonstrated that the adsorption process proceeds *via* a multi-step mechanism, where external mass transfer dominates the initial stage, followed by intraparticle diffusion at later stages. The PAR-Mg/Al LDH composite also exhibited good reusability over five consecutive adsorption–desorption cycles, maintaining high removal efficiency. These findings highlight the effectiveness of PAR-Mg/Al LDH as a promising adsorbent for the removal of anionic dyes from aqueous environments.

1. Introduction

The preservation of water resources against contamination by organic pollutants remains a paramount global challenge in the 21st century.[1,2] The rapid expansion of industries worldwide has led to the widespread release of synthetic dyes into aquatic ecosystems, causing significant ecological disruption and posing substantial risks to human health.[3–5] These dyes are extensively utilized in a myriad of sectors, including textiles, leather tanning, paper production, plastics, and cosmetics, due to their stability and vivid coloration.[6] However, this very stability, conferred by complex aromatic structures, renders them resistant to degradation by heat, light, and oxidizing agents, making them persistent environmental pollutants.[7] The discharge of dye-laden effluents into rivers, lakes, and groundwater is a common practice, leading to the reduction of light penetration in water bodies, which adversely affects photosynthetic activity and the aquatic food chain.[8]

Among these synthetic dyes, Acid Fuchsin (AF) is a particularly concerning anionic dye. Beyond its industrial applications, AF is known to be toxic, mutagenic, and carcinogenic.[9] While it

has been explored as a laboratory reagent and even studied for its *in vitro* inhibition of human immunodeficiency virus (HIV),[9] its hazardous nature necessitates effective removal from wastewater before discharge. Despite its toxicity, limited studies have focused on the systematic adsorption behavior and efficient removal of AF from aqueous environments, highlighting a critical research gap that this study aims to address.[10]

Various physicochemical techniques, such as coagulation, flocculation, membrane filtration, ion-exchange, and advanced oxidation, have been employed for dye removal from wastewater.[11–13] Among these, adsorption is widely recognized as a superior method due to its simplicity, cost-effectiveness, high efficiency—even at low contaminant concentrations—and the potential for adsorbent regeneration and reuse.[14,15] The efficacy of this process is predominantly governed by the selection and design of a high-performance adsorbent.[16–19]

In recent years, Layered Double Hydroxides (LDHs), also known as anionic clays, have emerged as a promising class of adsorbent materials.[20] Their structure is derived from brucite-like layers ($Mg(OH)_2$), where a partial isomorphous substitution of divalent cations (*e.g.*, Mg^{2+}, Zn^{2+}) with trivalent cations (*e.g.*, Al^{3+}, Fe^{3+}) generates positively charged sheets. This charge is balanced by interlayer anions (*e.g.*, CO_3^{2-}, NO_3^-, Cl^-) and water molecules, resulting in the general formula $[M^{2+}_{1-x}M^{3+}_x(OH)_2][A^{n-}]_{x/n}\cdot zH_2O$,

*Chemistry Department Faculty of Science, Mansoura University, Mansoura, Egypt.
E-mail: fathyawad949@yahoo.com; Tel: +00201000166374*

where *x* typically ranges from 0.2 to 0.4.[21] This unique architecture endows LDHs with high anion exchange capacity, tunable interlayer chemistry, and large surface areas, making them particularly effective for sequestering anionic pollutants.[22,23]

However, the performance of pristine LDHs can be constrained by their limited interlayer spacing and low density of specific functional sites. To overcome these limitations, intercalation with organic anions has proven to be an effective strategy for enhancing their adsorption properties and tailoring their affinity for specific contaminants.[22] 4-(2-Pyridylazo) resorcinol (PAR) is a well-known metallochromic indicator, traditionally used in spectrophotometric determinations and EDTA titrations of metal ions.[24–27] Its molecular structure, featuring azo groups, pyridine nitrogen, and phenolic hydroxyl groups, offers multiple active sites for interaction with pollutants. We hypothesize that intercalating PAR into the LDH gallery will not only expand the interlayer space but also introduce aromatic moieties and functional groups that can synergistically enhance the adsorption of aromatic dyes like Acid Fuchsin through mechanisms such as π–π stacking, hydrogen bonding, and electrostatic interactions.

Herein, we report the synthesis, comprehensive characterization, and application of a novel PAR-intercalated Mg/Al LDH (PAR-Mg/Al LDH) nanocomposite for the efficient adsorption of Acid Fuchsin from aqueous solutions. The specific objectives of this study are to: (1) synthesize and characterize PAR-Mg/Al LDH using techniques such as FTIR, XRD, SEM, EDX, and XPS; (2) evaluate the adsorption performance under varying operational parameters (pH, contact time, initial concentration, and temperature); (3) analyze the equilibrium, and kinetic data to understand the adsorption process; (4) investigate the reusability of the adsorbent and its efficacy in real water samples; (5) propose a plausible adsorption mechanism; and (6) explore a novel secondary application through molecular docking simulations to assess the potential interaction of Acid Fuchsin with the SARS-CoV-2 spike protein, providing a broader context for its biochemical relevance.

2. Experimental section

2.1. Materials

All chemicals used in this study were of analytical grade and employed without further purification. Magnesium chloride hexahydrate ($MgCl_2 \cdot 6H_2O$, 99%), aluminum chloride hexahydrate ($AlCl_3 \cdot 6H_2O$, 99%), sodium hydroxide (NaOH, 99%), and 4-(2-Pyridylazo) resorcinol (PAR) were procured from Sigma-Aldrich. Acid Fuchsin (AF) dye was supplied by the Dye Star Company, Brazil. All solutions were prepared using distilled water.

2.2. Synthesis of PAR intercalated Mg/Al LDH

The PAR-intercalated Mg/Al LDH composite was synthesized *via* a co-precipitation method followed by hydrothermal treatment. In a typical procedure, 0.3 g of PAR was dispersed in 30 mL of distilled water, which was selected as the optimal concentration for effective intercalation, and the mixture was sonicated for 15 minutes to obtain a homogeneous suspension. Preliminary

optimization experiments indicated that increasing the PAR concentration beyond this value did not result in further expansion of the LDH interlayer spacing; instead, excess PAR remained in the filtrate or preferentially adsorbed on the external surface rather than undergoing true intercalation. Excessive PAR loading may also induce steric hindrance or aggregation effects, which can disrupt layer ordering and limit the accessibility of active adsorption sites.

Subsequently, 1.0165 g of $MgCl_2 \cdot 6H_2O$ and 0.6035 g of $AlCl_3 \cdot 6H_2O$ (corresponding to a Mg/Al molar ratio of 2 : 1) were added to the PAR suspension, and the mixture was vigorously stirred for 2 hours at room temperature. The pH of the solution was then adjusted to 10.0 by dropwise addition of a 5.0 M NaOH solution under continuous stirring for 30 minutes. The resulting slurry was transferred into a 100 mL Teflon-lined stainless-steel autoclave and subjected to hydrothermal treatment at 150 °C for 24 hours. After natural cooling to room temperature, the solid product was collected by centrifugation, washed repeatedly with distilled water and ethanol to remove residual impurities, and finally dried overnight in an oven at 80 °C. For comparison, pristine Mg/Al LDH was prepared using an identical procedure in the absence of the PAR modifier.

2.3. Characterization

The synthesized materials were characterized using several analytical techniques. Fourier Transform Infrared (FTIR) spectra were recorded on a Bruker Tensor II spectrometer in the range of 400–4000 cm^{-1} to identify functional groups. X-Ray Diffraction (XRD) patterns were obtained using a Shimadzu XRD-7000 diffractometer with Cu Kα radiation ($\lambda = 1.5406$ Å) operating at 40 kV and 30 mA, to determine the crystalline structure and phase composition. The surface morphology and elemental composition were examined by Scanning Electron Microscopy (SEM) coupled with Energy-Dispersive X-ray spectroscopy (EDX) on a JEOL JSM-IT200 microscope. The surface charge was determined by measuring the Zeta potential using a Malvern Zetasizer Nano ZS. The surface chemical composition and states were analyzed by X-ray Photoelectron Spectroscopy (XPS) on a Thermo Scientific K-Alpha + spectrometer with a monochromatic Al Kα X-ray source.

2.4. Adsorption experiments

Batch adsorption experiments were conducted to evaluate the performance of the synthesized adsorbents for the removal of Acid Fuchsin (AF) from aqueous solutions. All experiments were performed in 100 mL glass tubes containing 50 mL of AF solution and a fixed adsorbent dose of 50 mg (1.0 g L^{-1}), unless otherwise specified. This adsorbent dosage was selected based on preliminary optimization experiments. Increasing the adsorbent dose beyond 1.0 g L^{-1} led to a higher removal efficiency; however, a decrease in adsorption capacity (mg g^{-1}) was observed due to particle aggregation and overlapping of active adsorption sites, which reduces the effective surface area available for dye uptake. The mixtures were agitated on an orbital shaker at 250 rpm. After each experiment, the suspensions were centrifuged, and the residual dye concentration in

the supernatant was determined using a UV-vis spectrophotometer (Shimadzu, UV-1800) at the maximum absorption wavelength of AF (λ_max = 546 nm). The influence of solution pH on adsorption was studied over a range of 2.0 to 10.0, with the initial AF concentration fixed at 100 mg L^{-1}. The pH was adjusted using 0.01 M HCl or NaOH solutions. Isotherm studies were carried out by varying the initial AF concentration from 1.0 to 800.0 mg L^{-1} while maintaining the solution pH at 4.0, temperature at 25 °C, and contact time of 2 hours. Adsorption kinetics were investigated at an initial AF concentration of 500 mg L^{-1} and pH 4.0, with samples collected at predetermined time intervals (5, 15, 30, 60, 120, 180, and 240 minutes). The impact of temperature on the adsorption process was evaluated at 25 °C, 40 °C, and 55 °C.

The adsorption capacity at equilibrium, q_e (mg g^{-1}), and the removal efficiency, E (%), were calculated using eqn (1) and (2), respectively:[28–30]

$$\text{Removal}(\%) = \frac{100(C_0 - C_\text{e})}{C_\text{e}} \tag{1}$$

$$q_\text{e} = (C_0 - C_\text{e}) \times \frac{V}{W} \tag{2}$$

where C_0 and C_e (mg L^{-1}) are the initial and equilibrium concentrations of AF, respectively, VV (L) is the volume of the solution, and mm (g) is the mass of the dry adsorbent used.

2.5. Desorption and reusability study

The reusability of the PAR-Mg/Al LDH adsorbent was assessed over five consecutive adsorption–desorption cycles. After the adsorption cycle, the dye-loaded adsorbent was separated by centrifugation. Desorption was carried out by stirring the spent adsorbent with 40 mL of 0.1 M NaOH solution as an eluent for 4 hours at 25 °C. The regenerated adsorbent was then separated, washed thoroughly with distilled water until neutral pH, dried at 80 °C, and reused in the subsequent adsorption cycle under the same initial conditions.

2.6. Analysis of real water samples

To evaluate the practical applicability of the adsorbent, its adsorption efficiency was examined using different real water samples spiked with a known concentration of Acid Fuchsin (AF, 50 mg L^{-1}). The investigated samples included tap water collected from the laboratory supply, Nile River water collected from the Giza area, Egypt, and domestic sewage water originating from kitchen wastewater. Prior to adsorption experiments, all real water samples were thoroughly filtered using standard filter paper to remove suspended solids and visible particulate matter. No additional physicochemical pretreatment was applied. The adsorption experiments were then carried out under the same conditions used for deionized water to allow direct comparison of adsorption performance.

2.7. Molecular docking study

Molecular docking simulations were performed to explore the potential interaction between Acid Fuchsin and the SARS-CoV-2 spike protein (PDB ID: 7JWY). The protein structure was prepared using the Molecular Operating Environment (MOE) 2015 software by removing water molecules and adding hydrogen atoms. The 3D structure of Acid Fuchsin was energy-minimized using the MMFF94x force field. The active site was identified using the "Site Finder" module. Docking calculations were carried out using the "Dock" module with the "London dG" scoring function to generate 30 potential binding poses. The receptor was kept rigid during the docking process. The resulting poses were analyzed for binding energy (kcal mol^{-1}) and interaction patterns with key amino acid residues.

3. Results and discussion

3.1. Characterization

The successful synthesis and surface characteristics of the pristine Mg/Al LDH and the modified PAR-Mg/Al LDH were confirmed through a series of analytical techniques including FTIR, XRD, SEM, EDX, Zeta potential, and XPS.

3.1.1. Fourier transform infrared (FTIR) spectroscopy.
The FTIR spectra of Mg/Al LDH and PAR-Mg/Al LDH are presented in Fig. 1A. The spectrum of pristine Mg/Al LDH exhibits a broad absorption band centered at approximately 3449 cm^{-1}, which is attributed to the O–H stretching vibrations of hydroxyl groups in the brucite-like layers and interlayer water molecules.[21] Upon intercalation with PAR, this band is retained with a slight shift, indicating the involvement of surface and interlayer hydroxyl groups in hydrogen bonding interactions with the organic modifier. Clear evidence for the successful incorporation of PAR into the LDH structure is provided by the appearance of new absorption bands in the PAR-Mg/Al LDH spectrum that are absent in pristine LDH. The band observed at 3088 cm^{-1} corresponds to aromatic C–H stretching vibrations, confirming the presence of PAR aromatic rings within the composite.[31] In addition, the band located at around 1629 cm^{-1}, originally associated with the H–O–H bending vibration of interlayer water, exhibits a noticeable shift after PAR intercalation. This shift is attributed to the overlap with C=C and C=N stretching vibrations of PAR, indicating strong interactions between PAR molecules and the LDH layers.[32] The characteristic nitrate stretching band of pristine LDH at 1361 cm^{-1} is significantly altered after modification, suggesting partial anion exchange between interlayer nitrate ions and PAR species during the intercalation process.[28] Furthermore, additional bands appearing at 1079 cm^{-1} and 747 cm^{-1} are assigned to C–O (or S=O) stretching and aromatic ring bending vibrations of PAR, respectively, providing further confirmation of its successful incorporation into the LDH galleries.[33] Importantly, a distinct band observed at approximately 954 cm^{-1} in both Mg/Al LDH and PAR-Mg/Al LDH spectra is attributed to M–OH (Mg–OH/Al–OH) bending vibrations of the brucite-like LDH layers. The retention of this band after PAR intercalation demonstrates that the fundamental layered structure of LDH is preserved and not disrupted by the modification process. The low-frequency region below 800 cm^{-1} is dominated by metal–oxygen lattice vibrations (O–Mg(Al)–O and Mg(Al)–OH), further confirming the structural integrity of the LDH framework.[34] Overall, the
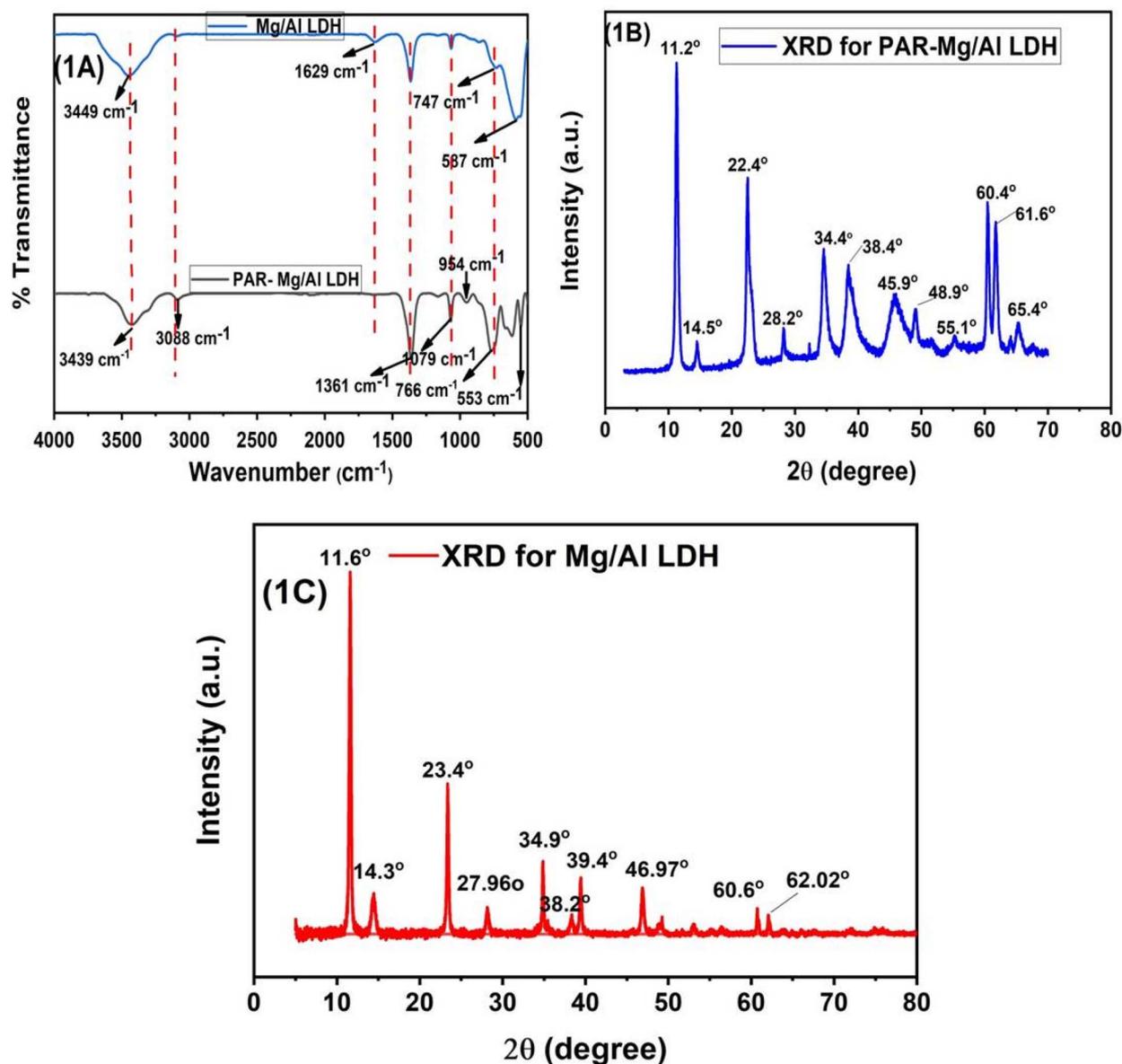
Fig. 1 (A) Fourier transform infrared spectra of Mg/Al LDH, and PAR-Mg/Al LDH. (B) XRD patterns of PAR-Mg/Al LDH. (C) XRD patterns of Mg/Al LDH.

FTIR results confirm not only the successful incorporation of PAR into the LDH structure through intercalation and surface interactions, but also the preservation of the brucite-like layered framework, with interactions occurring primarily *via* hydrogen bonding and anion exchange mechanisms.

3.1.2. X-ray diffraction (XRD) analysis. The XRD patterns were used to investigate the crystalline structure and changes in the interlayer geometry after modification. The patterns for PAR-Mg/Al LDH and Mg/Al LDH are shown in Fig. 1B and C, respectively. The pattern for PAR-Mg/Al LDH (Fig. 2B) exhibits the characteristic reflections of a well-defined layered double hydroxide structure. Sharp and symmetric peaks were observed at 2θ values of 11.2°, 22.4°, 34.4°, 38.4°, 45.9°, 60.4°, and 61.6°, which can be indexed to the (003), (006), (012), (015), (018),

(110), and (113) crystal planes of a hydrotalcite-like phase.[35–38] The presence of higher-order reflections such as (006) and (009) confirms a highly ordered layered structure. The basal spacing (d_{003}), calculated from the (003) reflection using Bragg's law, was found to be 0.79 nm for PAR-Mg/Al LDH. In comparison, the pristine Mg/Al LDH (Fig. 1C) showed its (003) peak at a higher 2θ angle of 11.6°, corresponding to a smaller d-spacing of 0.76 nm. This clear shift of the (003) peak to a lower angle (from 11.6° to 11.2°) upon PAR intercalation indicates an increase in the interlayer distance from 0.76 nm to 0.79 nm. This expansion is direct evidence that PAR molecules have been successfully intercalated into the interlayer gallery of the LDH, pushing the layers apart. The retention of sharp and well-defined peaks after modification confirms that the crystalline
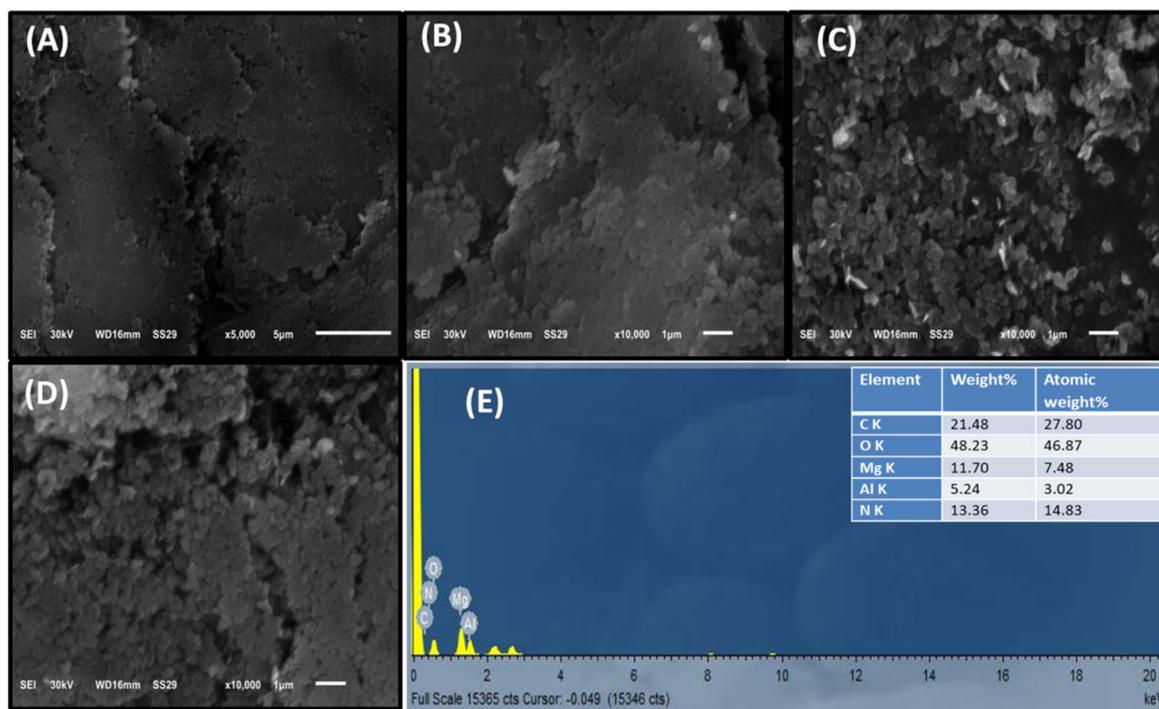
Fig. 2 SEM images of PAR-Mg/Al LDH from (A to D). (E) EDX spectrum of PAR-Mg/Al LDH.

framework of the LDH remains intact, demonstrating structural stability post-intercalation. The XRD data, therefore, conclusively proves the successful synthesis of a crystalline and ordered PAR-Mg/Al LDH composite with an expanded interlayer space, which is highly beneficial for accommodating dye molecules during adsorption.

3.1.3. Morphological and elemental analysis (SEM and EDX). The surface morphology and elemental composition of the synthesized PAR-Mg/Al LDH were investigated using Scanning Electron Microscopy (SEM) coupled with Energy-Dispersive X-ray Spectroscopy (EDX). The SEM micrographs (Fig. 2A–D) reveal the characteristic morphology of the layered double hydroxide. The images show agglomerates of plate-like particles with a well-defined layered structure, which is typical for LDH materials.[39] The particles exhibit a non-uniform size distribution and appear to form a porous, heterogeneous surface. This porous and layered morphology is highly advantageous for adsorption applications, as it provides a large surface area and multiple active sites for the uptake of pollutant molecules.[40] The observed structure confirms the successful formation of a layered composite, and the presence of these textural features is expected to facilitate the diffusion and binding of Acid Fuchsin dye molecules during the adsorption process.[41] To complement the morphological analysis, EDX spectroscopy was employed to determine the elemental composition of the PAR-Mg/Al LDH composite. The EDX spectrum (Fig. 2E) clearly identifies the presence of magnesium (Mg), aluminum (Al), oxygen (O), carbon (C), and nitrogen (N). The quantitative analysis gives the following weight percentages: C (21.48%), O (48.23%), Mg (11.70%), Al (5.24%), and N

(13.36%). The detection of Mg and Al confirms the backbone of the Mg/Al LDH structure. The significant presence of carbon (21.48%) and a substantial amount of nitrogen (13.36%) are not native to the pristine LDH and can be unequivocally attributed to the organic modifier, PAR. The high nitrogen content specifically supports the successful incorporation of the nitrogen-containing functional groups (e.g., azo group [–N═N–] and pyridyl nitrogen) from the PAR molecule into the composite. The oxygen signal originates from both the hydroxide layers of the LDH and possible oxygen-containing groups in PAR. Collectively, the EDX data provides strong evidence for the successful functionalization of the Mg/Al LDH with PAR, creating a hybrid organic-inorganic adsorbent.

3.1.4. Zeta potential analysis. The surface charge of the PAR-Mg/Al LDH composite was evaluated using zeta potential measurements. As depicted in Fig. S1, the material exhibits a zeta potential value of +10.8 mV at its natural pH. This positive surface charge unequivocally confirms that the composite's surface is positively charged, which is a characteristic feature of LDHs due to the presence of Mg^{2+} and Al^{3+} cations in the brucite-like layers, potentially augmented by protonated amine groups from the intercalated PAR molecules. This net positive charge is highly favorable for the electrostatic attraction and adsorption of anionic dyes like Acid Fuchsin. While the magnitude of +10.8 mV indicates a tendency for colloidal instability and potential particle aggregation in suspension over time,[42] it is sufficient for the short-term batch adsorption experiments conducted in this study. The positive nature of the surface remains the key factor governing the initial adsorption mechanism.

3.1.5. X-ray Photoelectron Spectroscopy (XPS) analysis. XPS analysis was conducted to probe the surface elemental composition and chemical states of the elements within the PAR-Mg/Al LDH composite. The wide-survey scan (Fig. 3A) confirms the presence of the expected elements: carbon (C), oxygen (O), magnesium (Mg), aluminum (Al), and nitrogen (N), consistent with the EDX results.

The high-resolution spectra provide detailed chemical insight: The Mg 1s peak at ~1304 eV and the Mg 2p peak at ~50 eV correspond to Mg^{2+} in Mg–O bonds, typical of the brucite-like layers (Fig. 3B).[43,44] The Al 2p peak at approximately 74 eV and the Al 2s peak at 119 eV are characteristic of Al^{3+} in an Al–O bonding environment, confirming its presence in the LDH framework (Fig. 3C).[43,44] The deconvolution of the C 1s spectrum (Fig. 3D) reveals multiple components: a dominant peak at ~284.6 eV (C–C/C–H), a peak at ~286.2 eV (C–O/C–N), and a peak at ~288.5 eV (O–C═O).[45] These signals originate from the aromatic and functional groups of the intercalated PAR molecule. The O 1s spectrum (Fig. 3E) can be fitted with contributions from metal–oxygen bonds (Mg–O, Al–O) at ~531 eV and hydroxyl groups (OH⁻) or water at higher binding energies (~532–533 eV).[44] The presence of a N 1s signal at around 400 eV (Fig. 3F) is a crucial indicator of successful PAR modification. The peak can be attributed to nitrogen in azo (–N═N–) and pyridyl groups from the PAR molecule.[29,32,46] The XPS data collectively provides definitive evidence for the successful synthesis of the PAR-Mg/Al LDH composite, confirming the coexistence of the inorganic LDH structure and the organic PAR modifier on the material's surface.

3.2. Dye adsorption studies

3.2.1. Effect of solution pH. The pH of the aqueous solution is a critical parameter in the adsorption process, as it governs the surface charge of the adsorbent and the ionization state of the dye molecules. The effect of pH on the adsorption of Acid Fuchsin (AF) onto both Mg/Al LDH and PAR-Mg/Al LDH was investigated over a pH range of 2.0 to 10.0, and the results are presented in Fig. 4A.

A clear trend was observed where the adsorption capacity for AF decreased with increasing pH for both adsorbents. The maximum adsorption occurred at pH 4.0. This pH-dependent behavior can be explained by the surface charge properties of the LDHs. In acidic medium (pH 2–4), the surface of the LDH is highly protonated, acquiring a strong positive charge. This creates a powerful electrostatic attraction with the negatively charged sulfonate groups (–SO₃⁻) of the AF dye molecules, leading to high removal efficiency.[9,47]

As the pH increases (5–7), the surface becomes less positively charged due to deprotonation, thereby weakening the electrostatic driving force and resulting in a gradual decrease in adsorption capacity. At alkaline pH levels (8–10), the LDH surface acquires a net negative charge, causing electrostatic repulsion with the anionic AF dye and a significant drop in adsorption.

Throughout the entire pH range, the PAR-Mg/Al LDH composite demonstrated superior adsorption performance compared to the pristine Mg/Al LDH. This enhanced efficiency can be attributed to the synergistic effects provided by the PAR intercalation. Beyond electrostatic interactions, the aromatic rings of PAR enable π–π stacking with the conjugate structure of AF. Furthermore, functional groups on PAR (e.g., –OH, –N═N–) can form hydrogen bonds and complexes with the dye, providing additional adsorption pathways that remain active even at near-neutral pH where electrostatic forces diminish. The
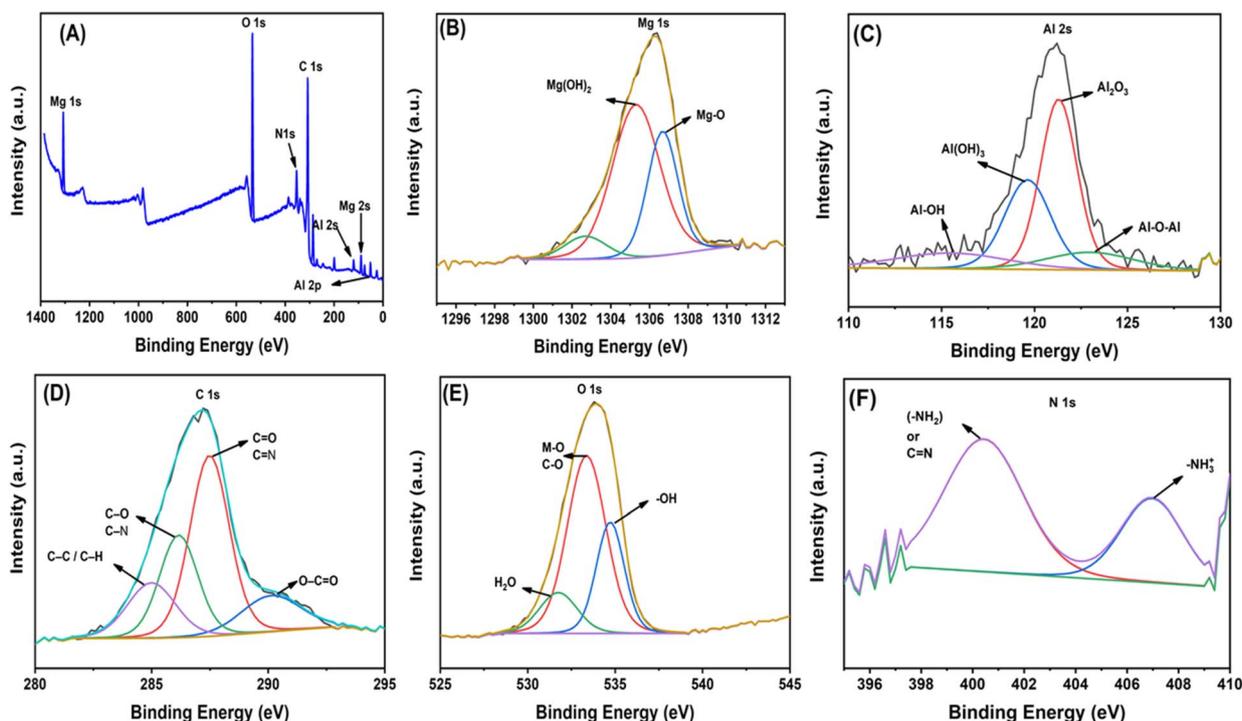

Fig. 3 XPS spectra PAR-Mg/Al LDH (A); high resolution XPS spectra of (B) Mg 1s, (C) Al 2s, (D) C 1s, (E) O 1s and (F) N 1s.
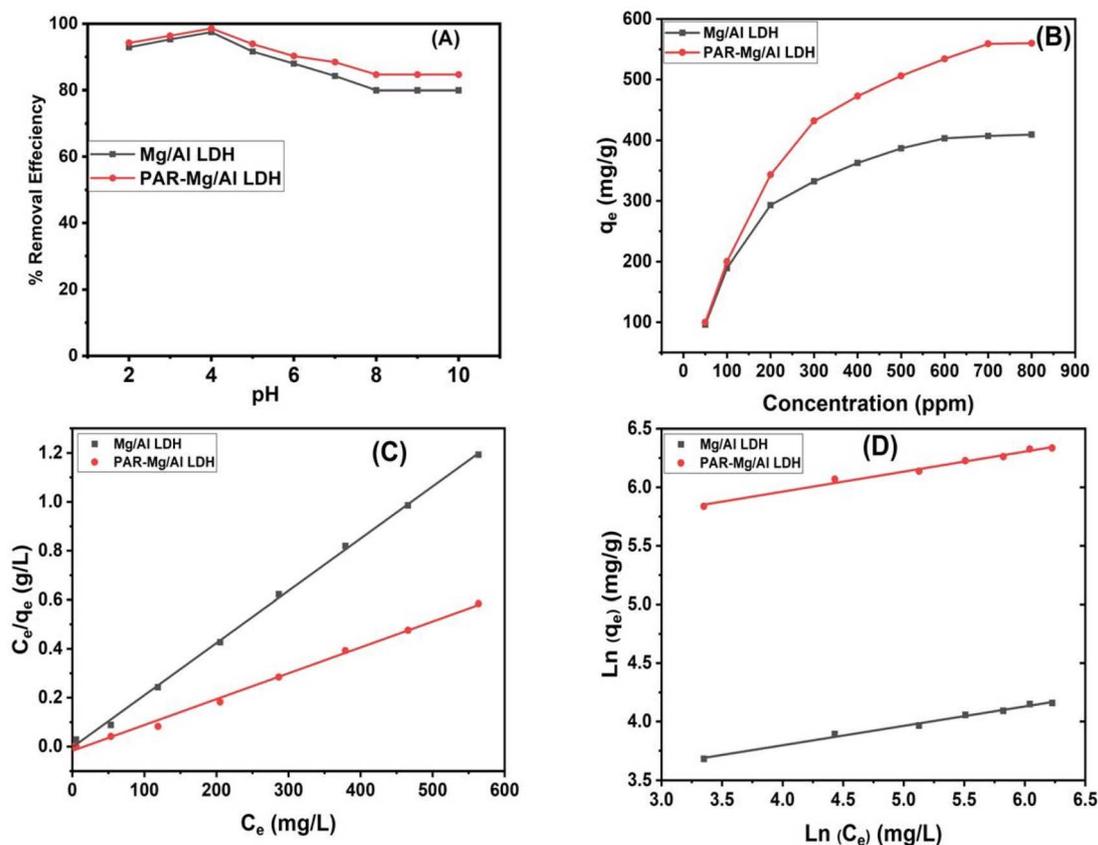
Fig. 4   The adsorption efficiency of PAR–Mg/Al LDH as a function of (A) pH; (B) concentration; (C) Langmuir isotherm model and (D) Freundlich isotherm model.

incorporation of PAR also potentially increases the surface area and provides more active sites, contributing to the overall improved performance of the composite adsorbent.

3.2.2.   Effect of initial dye concentration and adsorption isotherm. The effect of the initial Acid Fuchsin (AF) concentration on its adsorption by Mg/Al LDH and PAR-Mg/Al LDH was investigated over a concentration range of 1.0–800 mg L^{-1} at pH 4.0 and ambient temperature, as shown in Fig. 4B. The PAR-Mg/Al LDH composite exhibited nearly complete removal efficiency at initial AF concentrations up to 300 mg L^{-1}, which can be attributed to the high availability of active adsorption sites relative to dye molecules at lower concentrations. As the initial AF concentration increased from 1.0 to 800 mg L^{-1}, the equilibrium adsorption capacity (q_e) of both adsorbents increased markedly. This behavior is driven by the enhanced concentration gradient between the bulk solution and the adsorbent surface, which provides a stronger driving force for mass transfer and promotes increased dye uptake.[29,48,49] The pristine Mg/Al LDH displayed a gradual increase in adsorption capacity, reaching a maximum experimental q_e of approximately 406.0 mg g^{-1}. In contrast, the PAR-Mg/Al LDH composite showed a substantially higher adsorption capacity, attaining a maximum experimental q_e of approximately 560.0 mg g^{-1}. The enhanced adsorption performance of PAR-Mg/Al LDH can be attributed to the successful intercalation of PAR, which introduces additional functional groups, enhances electrostatic

attraction toward the anionic dye, and improves accessibility of adsorption sites. At concentrations approaching 800 mg L^{-1}, the adsorption capacity for both materials began to plateau, indicating the saturation of available binding sites and the approach of adsorption equilibrium. The clearly superior performance of PAR-Mg/Al LDH establishes it as a highly promising adsorbent for treating textile wastewater contaminated with anionic dyes (Table S1).

To quantitatively understand the adsorption equilibrium of Acid Fuchsin onto PAR-Mg/Al LDH, the experimental data were analyzed using two widely recognized isotherm models: Langmuir and Freundlich.[50,51] The Langmuir isotherm (eqn (3)) presupposes monolayer adsorption onto a surface with a finite number of identical and energetically equivalent sites, with no interaction between adsorbed molecules.[52]

$$\frac{C_e}{q_e} = \frac{1}{b \, Q_0} + \frac{C_e}{Q_0} \qquad (3)$$

$$\ln q_e = \ln K_f + \frac{1}{n} \ln C_e \qquad (4)$$

where q_e (mg g^{-1}) is the amount adsorbed at equilibrium, C_e (mg L^{-1}) is the equilibrium concentration, Q_m (mg g^{-1}) is the theoretical maximum monolayer adsorption capacity, and b (L mg^{-1}) is the Langmuir constant related to the affinity of binding sites.

The Freundlich isotherm (eqn (4)) is an empirical model applied to multilayer adsorption on heterogeneous surfaces. Where K_f ((mg g^{-1}) (L mg^{-1})$^{1/n}$) is the Freundlich constant indicative of adsorption capacity, and n is the heterogeneity factor representing adsorption intensity.

A key feature of the Langmuir model is the dimensionless separation factor, R_L, defined by eqn (5), which indicates the nature of the adsorption:[53]

$$R_L = \frac{1}{1 + bC_0} \qquad (5)$$

where C_0 is the highest initial dye concentration. R_L value between 0 and 1 signifies favorable adsorption.[54,55]

The fitted models are presented in Fig. 4C and D, with the corresponding parameters summarized in Table 1. The Langmuir model yielded a high correlation coefficient ($R^2 = 0.9896$), and the calculated maximum capacity ($Q_m = 568.18$ mg g^{-1}) was in excellent agreement with the experimental value ($\sim$560 mg g^{-1}). This close fit suggests that the adsorption predominantly occurs as a monolayer on a homogeneous surface. Furthermore, the R_L value calculated was 0.0192, which is much less than 1, confirming that the adsorption process is highly favorable. Although the Freundlich model showed a slightly lower fit ($R^2 = 0.9848$), its parameter $n = 5.92$ (which is greater than 1) also indicates a favorable adsorption process. A value of $n > 2$ is generally considered to represent good adsorption intensity,[31,56] reflecting a relatively strong interaction between the Acid Fuchsin dye and the PAR-Mg/Al LDH composite.

3.2.3. Adsorption kinetics. Understanding adsorption kinetics is essential for evaluating the rate of solute uptake and determining the equilibrium time. The effect of contact time on the adsorption of Acid Fuchsin (AF) onto PAR-Mg/Al LDH is illustrated in Fig. S2A. A rapid increase in adsorption capacity was observed during the initial 5 min, achieving more than 50% of the maximum uptake. This behavior can be attributed to the high availability of active adsorption sites and the strong concentration gradient at the solid–liquid interface.[31,57] Subsequently, the adsorption rate gradually decreased as the available active sites became occupied, approaching equilibrium after approximately 120 min. These results indicate the fast adsorption kinetics and high efficiency of PAR-Mg/Al LDH, which are advantageous for practical wastewater treatment applications.

To elucidate the adsorption kinetics and possible rate-controlling steps, the experimental data were analyzed using the pseudo-first-order (PFO) and pseudo-second-order (PSO) kinetic models. The linearized forms of the PFO and PSO models are expressed by eqn (6) and (7), respectively:[15]

$$\log (q_e - q_t) = \log q_e - \frac{K_1 t}{2.303} \qquad (6)$$

$$\frac{t}{q_t} = \frac{1}{K_2 q_e^2} + \frac{t}{q_e} \qquad (7)$$

where q_t and q_e (mg g^{-1}) are the adsorption capacities at time t and at equilibrium, respectively. k_1(min^{-1}) and k_2 (g mg^{-1} min^{-1}) are the rate constants of the PFO and PSO models, respectively.

The fitted kinetic plots are shown in Fig. S2B and S2C, and the corresponding parameters are summarized in Table 2. The PSO model exhibited a significantly higher correlation coefficient ($R^2 = 0.999$) compared to the PFO model. Moreover, the calculated equilibrium adsorption capacity (q_e) obtained from the PSO model (518.13 mg g^{-1}) was in excellent agreement with the experimental value (506 mg g^{-1}), whereas the PFO model showed a considerable deviation. These results indicate that the PSO model better describes the adsorption process, suggesting that chemisorption plays a dominant role, involving valence forces through the sharing or exchange of electrons between AF molecules and the surface functional groups of PAR-Mg/Al LDH.

Since kinetic models alone cannot distinguish the diffusion mechanism, further analysis was conducted using the intraparticle diffusion model to clarify the mass transfer behavior. Adsorption is generally a multistep process involving external surface adsorption, followed by intraparticle diffusion into the pores and interlayer galleries of the adsorbent, which may act as a rate-limiting step. The intraparticle diffusion model parameters were evaluated according to the equations described in Section S1.[5,58] As depicted in Fig. S3, the plot of q_t versus $t^{1/2}$ exhibited multilinear behavior, indicating that the adsorption process proceeds through multiple stages rather than a single diffusion-controlled step. The obtained parameters ($k_{id} = 17.16$ mg g^{-1} h$^{-0.5}$, C = 281.42, $R^2 = 0.847$) suggest that intraparticle diffusion contributes to the overall adsorption process but is not the sole rate-controlling mechanism. The initial sharper region corresponds to rapid external surface adsorption governed primarily by film diffusion, followed by a second linear region associated with intraparticle diffusion within the pores and interlayer spaces of the LDH structure. The final plateau represents the equilibrium stage, where diffusion slows due to saturation of active sites. The non-zero intercept (C) further confirms the significant contribution of boundary layer diffusion.[5,58] To further distinguish between film diffusion and intraparticle diffusion, the Boyd kinetic model was applied as described in Section S2.[59,60] Fig. S4 presents the plot of Bt versus time t. Although good linearity was obtained ($R^2 = 0.9949$), the plot did not pass through the origin (intercept = 0.363), indicating that external mass transfer (film diffusion) dominates the initial adsorption stage, while intraparticle diffusion becomes significant at later stages. These findings confirm that

Table 1 Isotherm parameters for the removal of acid fuchsin dye by PAR-Mg/Al LDH

	Freundlich parameters				Langmuir parameters			
Dye	$1/n$	K_F	R^2	Q_{exp} (mg g^{-1})	$Q_{max\ fitted}$ (mg g^{-1})	R_L	B (L mg^{-1})	R^2
Acid fuchsin	0.1689	197.89	0.9848	560	568.18	0.0192	0.0637	0.989

Table 2   Parameters of PSO and PFO models for the adsorption of acid fuchsin anionic dye onto PAR-Mg/Al LDH

Dye	q_{eexp}(mg g^{-1})	PFO	Parameters			PSO	Parameters	
		R^2	q_{ecal}(mg g^{-1})	K_1 (min^{-1})		R^2	q_{ecal} (mg g^{-1})	K_2 (g mol^{-1} min^{-1})
Acid fuchsin	506	0.975	189.64	0.00029		0.999	518.13	0.00041

the adsorption of Acid Fuchsin onto PAR-Mg/Al LDH is governed by a combined diffusion mechanism rather than a single rate-limiting step.[5]

3.2.4.   Effect of interfering ions. The presence of competing anions in industrial wastewater can significantly influence the adsorption efficiency of anionic dyes. The effect of various interfering ions (Cl$^-$, NO$_3^-$, SO$_4^{2-}$, and PO$_4^{3-}$) on the removal of Acid Fuchsin by PAR-Mg/Al LDH was investigated, and the results are presented in Fig. S3.

A clear trend was observed in the removal efficiency: Cl$^-$ > NO$_3^-$ > SO$_4^{2-}$ > PO$_4^{3-}$. This trend is directly correlated with the charge and affinity of the competing anions for the positively charged LDH surface. Chloride (Cl$^-$) showed the least interference, maintaining the highest dye removal. As a monovalent anion with low charge density and weak affinity, it competes ineffectively with the AF dye molecules for adsorption sites. Nitrate (NO$_3^-$) caused a slight reduction in removal compared to Cl$^-$. Although also monovalent, its higher hydration energy and specific interaction properties result in slightly stronger competition. Sulfate (SO$_4^{2-}$) led to a noticeable decrease in adsorption efficiency. Its divalent nature gives it a stronger electrostatic attraction to the LDH layers, enabling it to compete more effectively for the available positive sites and anion exchange positions. Phosphate (PO$_4^{3-}$) exhibited the most significant inhibitory effect, resulting in the lowest dye removal. The trivalent charge and high affinity of phosphate anions cause them to form strong inner-sphere complexes with the LDH layers, effectively displacing pre-adsorbed dye molecules and blocking active sites.

These findings confirm that the adsorption of AF onto PAR-Mg/Al LDH occurs primarily through electrostatic attraction and anion exchange mechanisms. The competition follows the Hofmeister series, where anions with higher charge density and lower hydration energy possess a greater competitive advantage, thereby reducing the adsorption capacity for the target dye.

3.2.5.   Adsorption mechanism. To elucidate the adsorption mechanism of Acid Fuchsin onto PAR-Mg/Al LDH, FTIR analysis of the adsorbent was conducted before and after adsorption (Fig. 5A). The comparative spectra reveal significant changes that confirm the involvement of multiple interaction pathways.

The broad O–H stretching band shifted from 3450 cm^{-1} to 3412 cm^{-1} with decreased intensity, indicating strengthened hydrogen bonding between the LDH's surface hydroxyl groups and functional groups of the dye molecule. The H–O–H bending vibration at 1634.7 cm^{-1} shifted to 1652.8 cm^{-1}, suggesting possible π–π interactions between aromatic rings or new hydrogen bond formation. Characteristic peaks in the 1554–1360 cm^{-1} region showed subtle shifts, implying interactions between dye functional groups and metal centers. The emergence

of new peaks at 1226.7, 1107, and 1041.7 cm^{-1} corresponds to C–N and S=O vibrations from the adsorbed dye. Shifts in the low-frequency metal–oxygen vibrations further confirm coordination between dye molecules and the LDH framework.

Based on collective evidence from FTIR, zeta potential, pH studies, and interference experiments, the adsorption occurs through a synergistic combination of electrostatic attraction between the positively charged LDH surface and anionic dye groups, anion exchange with interlayer species, hydrogen bonding with surface hydroxyls, π–π stacking with aromatic rings of PAR, and potential complexation with metal cations in the LDH layers, as illustrated in Fig. 6. This multi-mechanistic approach explains the composite's exceptional adsorption performance.

3.2.6.   Performance in real water samples. To assess the practical applicability of PAR-Mg/Al LDH, its adsorption performance was evaluated using different real water samples spiked with 50 mg L^{-1} of Acid Fuchsin (AF). As shown in Fig. 5B, the composite exhibited high removal efficiency in all tested matrices, including tap water, Nile River water, domestic wastewater, and domestic sewage water. All real water samples were filtered prior to use to remove suspended particulate matter, as described in the experimental section. Compared with deionized water, a slight variation in removal efficiency was observed in real water matrices, which can be attributed to the presence of dissolved ions and residual organic matter that may compete with AF molecules for available adsorption sites. Nevertheless, PAR-Mg/Al LDH maintained effective adsorption performance under the tested conditions, demonstrating a good tolerance toward matrix complexity. All experiments were performed in triplicate, and the relative standard deviation (RSD) values were below 4%, indicating good reproducibility and reliability of the results. It should be noted that the reported removal efficiencies represent adsorption performance under the specific experimental conditions employed in this study and should be regarded as indicative rather than absolute values. Despite these limitations, the results provide preliminary evidence supporting the potential applicability of PAR-Mg/Al LDH for anionic dye removal in realistic water matrices.

3.2.7.   Reusability and regeneration. The reusability of an adsorbent is a critical economic and environmental factor for its practical application. The regeneration capability of PAR-Mg/Al LDH was investigated over five consecutive adsorption–desorption cycles using 0.1 M NaOH as the eluent. The results, presented in Fig. 5C, show that the adsorbent maintained a high removal efficiency of approximately 96.0% even after the fifth cycle. The FTIR spectrum of the regenerated adsorbent (after 5 cycles) showed no significant structural changes, confirming its chemical stability.
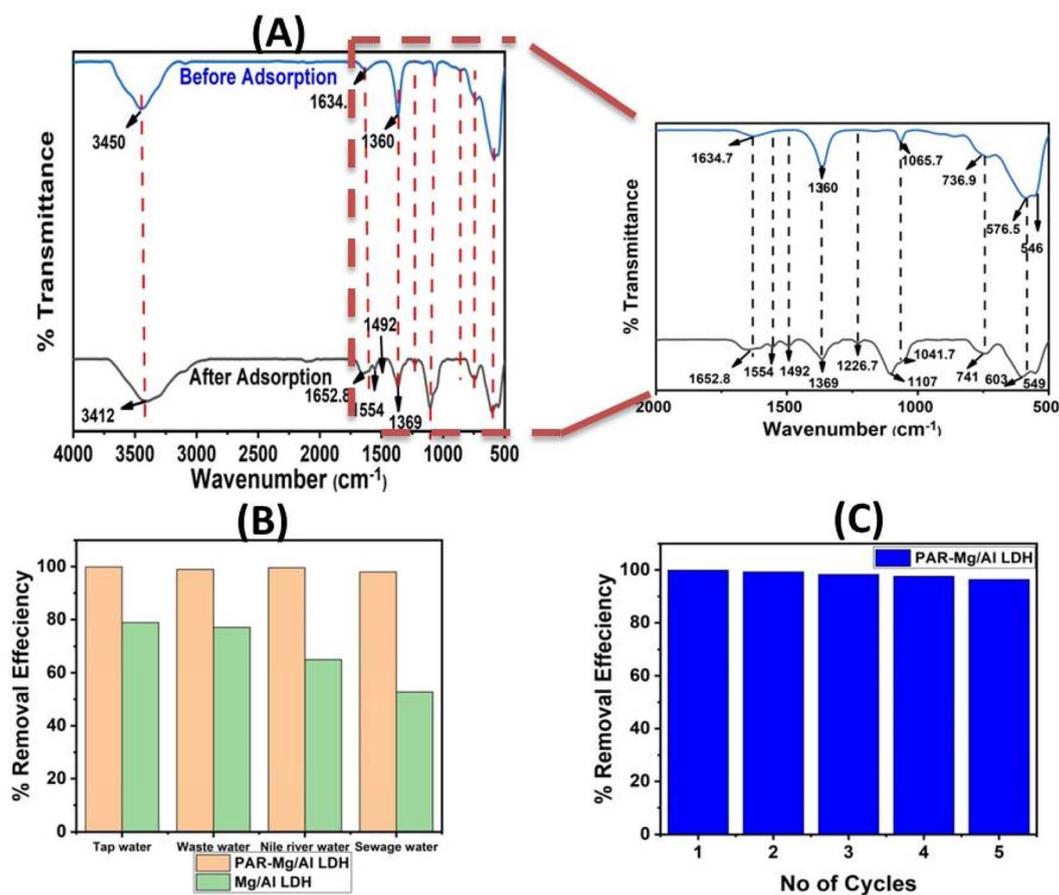
Fig. 5 (A) FTIR spectra of PAR-Mg/Al LDH before and after acid fuchsin dye adsorption; (B) real water samples analysis and (C) reusability of PAR-Mg/Al LDH adsorbent.

The slight gradual decline in efficiency is common for LDH-based adsorbents and can be attributed to several factors: (1) the partial retention of dye molecules within the interlayer spaces, (2) minor structural alterations or partial dissolution during the alkaline regeneration process, and (3) a marginal loss of active sites. The effective desorption is achieved because
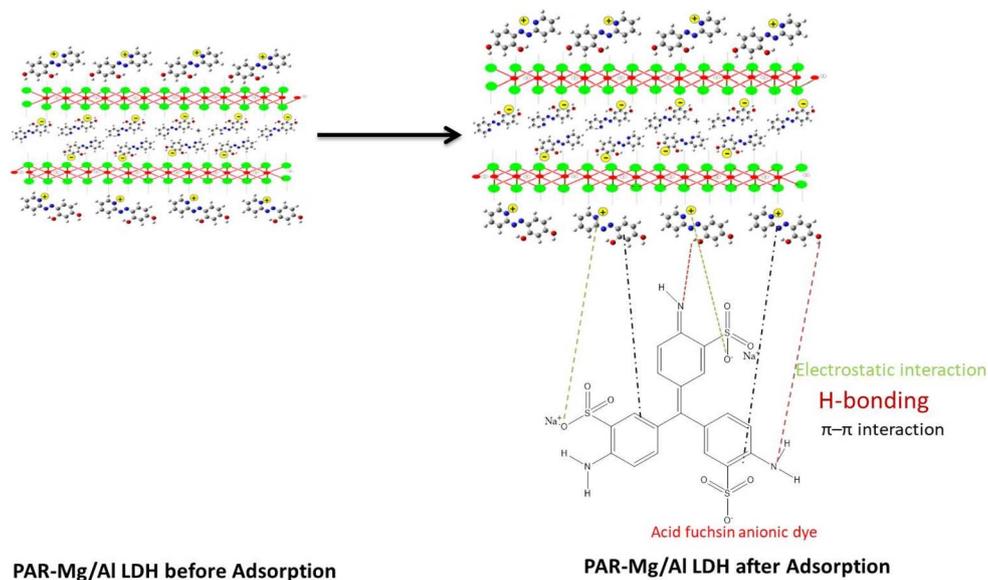

Fig. 6 Possible mechanisms for acid fuchsin dye adsorption onto PAR-Mg/Al LDH.
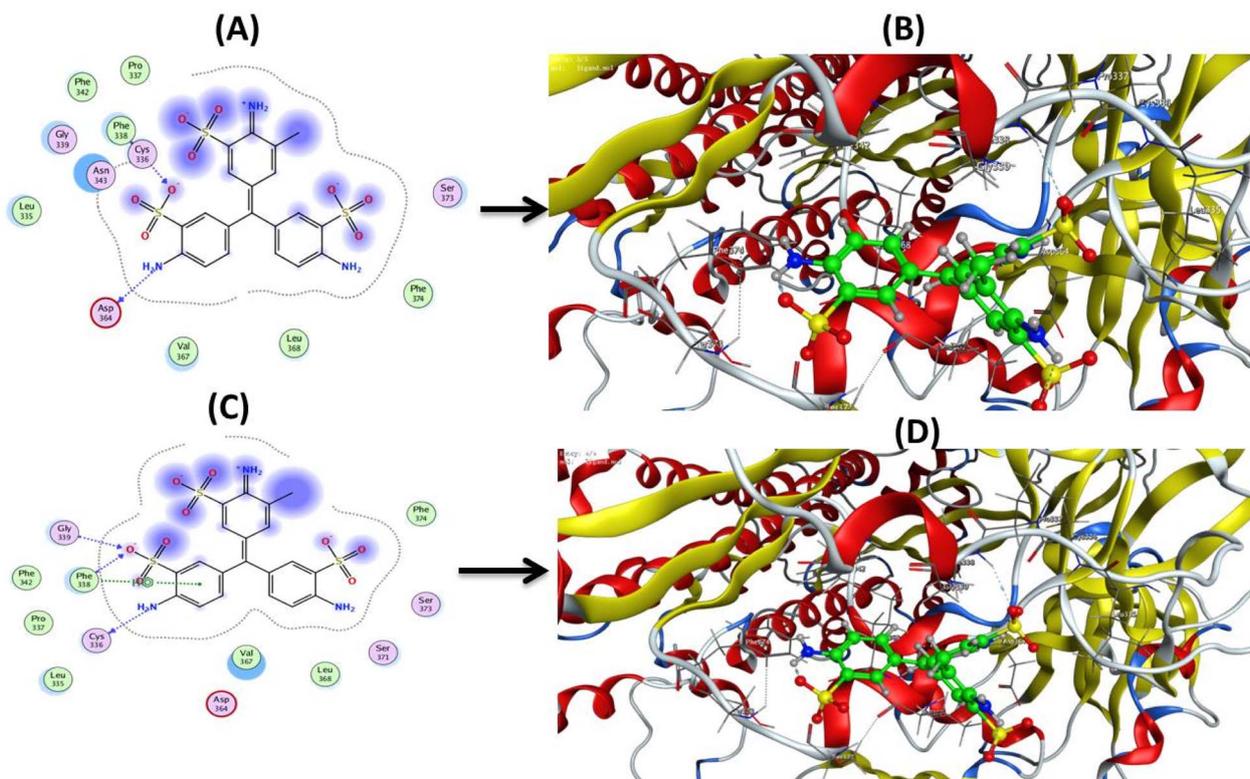
Fig. 7 Interaction diagram showing acid fuchsin dye docking interactions with7JWY protein (A) and (C). The 2D interaction of acid fuchsin with ACE2 receptor of SARS-CoV-2.(B) and (D). The 3D interaction of acid fuchsin with ACE2 receptor of SARS-CoV-2.

the high concentration of OH^- ions in NaOH solution competes with the dye anions for adsorption sites *via* ion-exchange and creates electrostatic repulsion against the negatively charged dye molecules. The excellent reusability demonstrated over five cycles establishes PAR-Mg/Al LDH as an economically and environmentally sustainable adsorbent for long-term use in wastewater treatment.

3.3. Molecular docking study

To explore a potential secondary application of Acid Fuchsin (AF), molecular docking simulations were performed to investigate its interaction with the SARS-CoV-2 spike protein (PDB ID: 7JWY) using MOE 2015 software. The 7JWY protein was selected due to its biological significance as part of the viral spike protein's receptor-binding domain (RBD), which mediates host cell entry and represents a key target for therapeutic intervention.[61] The well-characterized and readily available structure of this protein makes it highly suitable for computational studies. The protein structure was prepared by removing water molecules and adding hydrogen atoms, while the AF ligand geometry was optimized using the MMFF94x force field. The active site was identified using the Site Finder module, and docking calculations were carried out using the Dock module with the London dG scoring function, generating 30 binding poses while keeping the receptor rigid. The docking results, summarized in Table S3, revealed that AF exhibited a favorable binding energy of −5.69 kcal mol^{-1}, indicating a spontaneous interaction with the target. Analysis of the interaction profile identified specific

contacts within the protein's active pocket. Two primary hydrogen bonds were observed: one between the N13 atom of AF and the oxygen of ASP364 (3.22 Å, −2.1 kcal mol^{-1}), and another between the O12 atom of AF and the nitrogen of PHE338 (3.38 Å, −1.2 kcal mol^{-1}). Additional stabilization was provided by an interaction with GLY339 (3.03 Å, −4.4 kcal mol^{-1}) and a π–H bond with PHE338 (4.03 Å, −0.6 kcal mol^{-1}). These residues are critically involved in the host-virus recognition interface, suggesting that AF could potentially interfere with the spike-ACE2 complex formation (Fig. 7). The docking poses demonstrated good convergence with RMSD values of 1.22 Å and 1.70 Å, confirming the reliability of the predicted binding orientation. The lowest-energy pose formed a compact and stable complex stabilized by both hydrogen bonding and hydrophobic contacts. While molecular docking has inherent limitations, particularly regarding the precise correlation between scoring functions and experimental binding affinities,[62,63] these computational results strongly suggest that Acid Fuchsin could act as a moderate inhibitor of the SARS-CoV-2 spike protein by effectively interacting with key residues (ASP364, PHE338, GLY339) essential for structural stability and ligand recognition.[64,65] It should be emphasized that these findings are based solely on *in silico* molecular docking simulations and are intended to provide preliminary theoretical insight into the possible interaction of Acid Fuchsin with the viral spike protein. No experimental antiviral assays were conducted, and therefore no direct biological or antiviral activity can be concluded from this study.

4. Conclusions

In this study, a novel PAR-intercalated Mg/Al layered double hydroxide (PAR-Mg/Al LDH) was successfully synthesized and applied for the efficient removal of the anionic dye Acid Fuchsin (AF) from aqueous solutions. Comprehensive characterization using FTIR, XRD, SEM, EDX, and XPS confirmed the successful intercalation of PAR into the LDH interlayers, which effectively enhanced the adsorption properties of the material. The PAR-Mg/Al LDH composite exhibited a significantly higher maximum adsorption capacity (568.18 mg g^{-1}) than pristine Mg/Al LDH, as described by the Langmuir isotherm model, indicating mono-layer adsorption on a homogeneous surface. The adsorption process was strongly dependent on solution pH, with optimal removal observed at pH 4.0, where electrostatic attraction between the positively charged adsorbent surface and the anionic dye molecules is maximized. Kinetic analysis demonstrated that the adsorption followed a pseudo-second-order model, suggesting that chemisorption plays a dominant role in the uptake process. Importantly, intraparticle diffusion and Boyd model analyses revealed that the adsorption mechanism is governed by a combined diffusion process, in which film diffusion dominates the initial adsorption stage, while intraparticle diffusion becomes significant at later stages. The overall adsorption mechanism was attributed to the combined contributions of electrostatic attraction, anion exchange, hydrogen bonding, and π–π interactions. Furthermore, the composite exhibited excellent practical performance, maintaining high removal efficiency (>99%) in various real water matrices and demonstrating outstanding reusability over five consecutive adsorption–desorption cycles with minimal loss in efficiency. Additionally, molecular docking simulations provided preliminary theoretical insight into the possible interaction between Acid Fuchsin and the SARS-CoV-2 spike protein; however, this observation is limited to computational prediction and requires further experimental validation. Overall, PAR-Mg/Al LDH represents a highly efficient, reusable, and multifunctional adsorbent with promising potential for the remediation of anionic dyes in wastewater treatment applications.

Conflicts of interest

The authors declare no conflict of interest.

Data availability

All data generated or analyzed during this study are included in the main article and supplementary material (SI). Supplementary information: Zeta Potential of PAR-Mg/Al LDH (Fig. S1). Remediation of various anionic dyes using MgAl LDHS and/or organic compounds prepared through different reported methods. (Table S1). The adsorption capacity of PAR-Mg/Al LDH as a function of contact time (Fig. S2A) (B) PSO kinetic model (Fig. S2B). PFO kinetic model (Fig. S2C). Effect of interfering anions on acid fuchsin dye adsorption onto PAR-Mg/Al LDH (Fig. S3). Intraparticle Diffusion Model (S1). Intraparticle diffusion plots for the adsorption of Acid Fuchsin on PAR-Mg/Al LDH (Fig. S3.). Boyd Kinetic Model (S2). Boyd plot (Bt *versus t*) for the adsorption of Acid Fuchsin on PAR-Mg/Al LDH (Fig. S4.). The docking interaction parameters of acid fuchsin with 7JWY: VIRAL PROTEIN / 7JWYCOVID -19 (Table S2). See DOI: https://doi.org/10.1039/d5ra08890a.

References

1 J. C. Sousa, A. R. Ribeiro, M. O. Barbosa, M. F. R. Pereira and A. M. Silva, *J. Hazard. Mater.*, 2018, **344**, 146–162.
2 J. Karpińska and U. Kotowska, *Journal*, 2019, **11**, 2017.
3 D.-P. Häder, A. T. Banaszak, V. E. Villafañe, M. A. Narvarte, R. A. González and E. W. Helbling, *Sci. Total Environ.*, 2020, **713**, 136586.
4 M. K. Gupta, P. K. Tandon and N. Shukla, in *Nanostructured Materials for Treating Aquatic Pollution*, Springer, 2019, pp. 225–242.
5 A. El-Wakil, W. Abou El-Maaty and F. Awad, *J. Anal. Bioanal. Tech.*, 2014, **5**, 1–14.
6 G. Ameen, *Chemistry for the Life*, 2023, p. 213.
7 Z. U. Ahmad, *Synthesis and Characterization of Novel Functionalized Ordered Mesoporous Carbon (Omc) for Resorcinol and Sunset Yellow Removal*, University of Louisiana at Lafayette, 2019.
8 K. Knee and A. Paytan, *Treatise Estuar. Coast. Sci.*, 2011, **4**, 205–234.
9 N. Gong, Y. Liu and R. Huang, *Int. J. Biol. Macromol.*, 2018, **115**, 580–589.
10 A. A. Renita, P. S. Kumar and S. A. Jabasingh, *Bioresour. Technol. Rep.*, 2019, **7**, 100300.
11 T. Robinson, G. McMullan, R. Marchant and P. Nigam, *Bioresour. Technol.*, 2001, **77**, 247–255.
12 Q. Jiuhui, *J. Environ. Sci.*, 2008, **20**, 1–13.
13 A. M. Bakry, N. Amri, M. S. Adly, A. A. Alamri, R. S. Salama, A. M. Jabbari, M. S. El-Shall and F. S. Awad, *Sci. Rep.*, 2024, **14**, 18848.
14 A. A. Alqadami, S. M. Wabaidur, B.-H. Jeon and M. A. Khan, *Biomass Convers. Biorefin.*, 2024, **14**, 15757–15768.
15 F. Al-Qarhami, M. E. Khalifa, A. Abdallah and F. S. Awad, *Int. J. Biol. Macromol.*, 2025, **303**, 140744.
16 I. Ali, O. M. Alharbi, Z. A. ALOthman, A. Alwarthan and A. M. Al-Mohaimeed, *Int. J. Biol. Macromol.*, 2019, **132**, 244–253.
17 I. Ali, O. M. Alharbi, Z. A. ALOthman, A. M. Al-Mohaimeed and A. Alwarthan, *Environ. Res.*, 2019, **170**, 389–397.
18 M. A. Khan, S. M. Wabaidur, M. R. Siddiqui, A. A. Alqadami and A. H. Khan, *J. Cleaner Prod.*, 2020, **244**, 118867.
19 M. Moheb, A. M. El-Wakil and F. S. Awad, *Food Chem.*, 2025, 145411.
20 I. Mohiuddin, A. Grover, J. S. Aulakh, A. K. Malik, S. S. Lee, R. J. Brown and K.-H. Kim, *J. Hazard. Mater.*, 2021, **401**, 123782.
21 F. Cavani, F. Trifirò and A. Vaccari, *Catal. Today*, 1991, **11**, 173–301.
22 Y.-H. Chuang, C.-H. Liu, Y.-M. Tzou, J.-S. Chang, P.-N. Chiang and M.-K. Wang, *Colloids Surf., A*, 2010, **366**, 170–177.

23 F. Bruna, R. Celis, M. Real and J. Cornejo, *J. Hazard. Mater.*, 2012, **225**, 74–80.

24 G. Schwarzenbach and H. Flaschka, *Complexometric Titrations*, Methuen & Co. Ltd, London, 2nd edn, 1969, p. 490.

25 F. Pollard, P. Hanson and W. Geary, *Anal. Chim. Acta*, 1959, **20**, 26–31.

26 J. B. Hunt, S. H. Neece and A. Ginsburg, *Anal. Biochem.*, 1985, **146**, 150–157.

27 K. Low and C. Lee, *Bioresour. Technol.*, 1997, **61**, 121–125.

28 S. M. Waly, A. M. El-Wakil, W. M. Abou El-Maaty and F. S. Awad, *RSC Adv.*, 2024, **14**, 15281–15292.

29 S. M. Waly, A. M. El-Wakil, W. M. Abou El-Maaty and F. S. Awad, *New J. Chem.*, 2025, **49**, 1314–1324.

30 S. M. Waly, A. M. El-Wakil, M. M. Waly, W. M. A. El-Maaty and F. S. Awad, *Sci. Rep.*, 2025, **15**, 15555.

31 J.-C. Zheng, H.-M. Feng, M. H.-W. Lam, P. K.-S. Lam, Y.-W. Ding and H.-Q. Yu, *J. Hazard. Mater.*, 2009, **171**, 780–785.

32 N. M. Ghazy, E. A. Ghaith, Y. Abou El-Reash, R. R. Zaky, W. M. Abou El-Maaty and F. S. Awad, *RSC Adv.*, 2022, **12**, 35587–35597.

33 R. Wang, J. Zhu, S. Rastan and F. Haghighat, *J. Hazard. Mater.*, 2011, **192**, 1026–1032.

34 A. Inoue and M. Utada, *Clays Clay Miner.*, 1983, **31**, 401–412.

35 Y. Peng, Y. Sun, A. Hanif, J. Shang, Z. Shen, D. Hou, Y. Zhou, Q. Chen, Y. S. Ok and D. C. Tsang, *J. Cleaner Prod.*, 2021, **289**, 125142.

36 R. Li, J. J. Wang, B. Zhou, M. K. Awasthi, A. Ali, Z. Zhang, L. A. Gaston, A. H. Lahori and A. Mahar, *Sci. Total Environ.*, 2016, **559**, 121–129.

37 A. Matei, R. Birjega, A. Vlad, C. Luculescu, G. Epurescu, F. Stokker-Cheregi, M. Dinescu, R. Zavoianu and O. Pavel, *Appl. Phys. A*, 2013, **110**, 841–846.

38 Y. Cao, D. Zheng, S. Dong, F. Zhang, J. Lin, C. Wang and C. Lin, *J. Electrochem. Soc.*, 2019, **166**, C3106.

39 L. Ai, C. Zhang and L. Meng, *J. Chem. Eng. Data*, 2011, **56**, 4217–4225.

40 A. I. Khan and D. O'Hare, *J. Mater. Chem.*, 2002, **12**, 3191–3198.

41 J. Kameliya, A. Verma, P. Dutta, C. Arora, S. Vyas and R. S. Varma, *Inorganics*, 2023, **11**, 121.

42 Á. V. Delgado, F. González-Caballero, R. Hunter, L. Koopal and J. Lyklema, *J. Colloid Interface Sci.*, 2007, **309**, 194–224.

43 F. Zhang, C.-L. Zhang, L. Song, R.-C. Zeng, L.-Y. Cui and H.-Z. Cui, *Acta Metall. Sin. (Engl. Lett.)*, 2015, **28**, 1373–1381.

44 G. Zheng, C. Wu, J. Wang, S. Mo, Z. Zou, B. Zhou and F. Long, *Nanoscale Res. Lett.*, 2019, **14**, 281.

45 S. M. Waly, A. M. El-Wakil, W. M. Abou El-Maaty and F. S. Awad, *J. Saudi Chem. Soc.*, 2021, **25**, 101296.

46 A. M. El-Wakil, S. M. Waly, W. M. Abou El-Maaty, M. M. Waly, M. Yılmaz and F. S. Awad, *ACS omega*, 2022, **7**, 6058–6069.

47 L. Yang, Z. Shahrivari, P. K. Liu, M. Sahimi and T. T. Tsotsis, *Ind. Eng. Chem. Res.*, 2005, **44**, 6804–6815.

48 X. Qi, Q. Zeng, X. Tong, T. Su, L. Xie, K. Yuan, J. Xu and J. Shen, *J. Hazard. Mater.*, 2021, **402**, 123359.

49 F. S. Awad, A. M. Bakry, A. A. Ibrahim, A. Lin and M. S. El-Shall, *Ind. Eng. Chem. Res.*, 2021, **60**, 12675–12688.

50 F. S. Awad, K. M. AbouZied, W. M. Abou El-Maaty, A. M. El-Wakil and M. S. El-Shall, *Arabian J. Chem.*, 2020, **13**, 2659–2670.

51 S. Pourbeyram, *Ind. Eng. Chem. Res.*, 2016, **55**, 5608–5617.

52 M. Moheb, A. M. El-Wakil and F. S. Awad, *RSC Adv.*, 2025, **15**, 674–687.

53 F. Al-Qarhami, A. Abdallah, M. E. Khalifa and F. S. Awad, *Int. J. Biol. Macromol.*, 2025, 143459.

54 F. A. Pavan, A. C. Mazzocato and Y. Gushikem, *Bioresour. Technol.*, 2008, **99**, 3162–3165.

55 M. S. Alhumaimess, *Sep. Sci. Technol.*, 2020, **55**, 1303–1316.

56 S. Zamindar, S. Mandal, M. Murmu and P. Banerjee, *Mater. Adv.*, 2024, **5**, 4563–4600.

57 D. Borah, S. Satokawa, S. Kato and T. Kojima, *J. Colloid Interface Sci.*, 2008, **319**, 53–62.

58 W. J. Weber Jr and J. C. Morris, *J. Sanit. Eng. Div.*, 1963, **89**, 31–59.

59 G. Boyd, A. Adamson and L. Myers Jr, *J. Am. Chem. Soc.*, 1947, **69**, 2836–2848.

60 D. Reichenberg, *J. Am. Chem. Soc.*, 1953, **75**, 589–597.

61 M. H. Sampangi-Ramaiah, R. Vishwakarma and R. U. Shaanker, *Curr. Sci.*, 2020, **118**, 1087–1092.

62 J. Fan, A. Fu and L. Zhang, *Quant. Biol.*, 2019, **7**, 83–89.

63 G. M. Morris and M. Lim-Wilby, in *Molecular Modeling of Proteins*, Springer, 2008, pp. 365–382.

64 W. Dai, B. Zhang, X.-M. Jiang, H. Su, J. Li, Y. Zhao, X. Xie, Z. Jin, J. Peng and F. Liu, *Science*, 2020, **368**, 1331–1335.

65 Z. Xia, M. Sacco, Y. Hu, C. Ma, X. Meng, F. Zhang, T. Szeto, Y. Xiang, Y. Chen and J. Wang, *ACS Pharmacol. Transl. Sci.*, 2021, **4**, 1408–1421.